Synthesis and Calculations of Wurtzite $Al_{1-x}Gd_xN$ Heterostructural Alloys

Rebecca W. Smaha,*,§ Keisuke Yazawa,§ Andrew G. Norman, John S. Mangum, Harvey Guthrey, Geoff L. Brennecka, Andriy Zakutayev, Sage R. Bauers, Prashun Gorai,* and Nancy M. Haegel*

ABSTRACT: $Al_{1-x}Gd_xN$ is one of a series of novel heterostructural alloys involving rare earth cations with potentially interesting properties for (opto)electronic, magnetic, and neutron detector applications. Using alloy models in conjunction with density functional theory, we explored the full composition range for $Al_{1-x}Gd_xN$ and found that wurtzite is the ground-state structure up to a critical composition of $x_c = 0.82$. The calculated temperature-composition phase diagram reveals a large miscibility gap inducing spinodal decomposition at equilibrium conditions, with higher Gd substitution (meta)stabilized at higher temperatures. By depositing combinatorial thin films at high effective temperatures using radio-frequency cosputtering, we have achieved the highest Gd^{3+} incorporation into the wurtzite phase reported to date, with single-phase compositions at least up to $x \approx 0.25$ confirmed by high-resolution synchrotron grazing incidence wide-angle X-ray scattering. High-resolution transmission electron microscopy on material with $x \approx 0.13$ and $x \approx 0.24$ confirmed a uniform composition polycrystalline film with uniform columnar grains having the wurtzite structure. Spectroscopic ellipsometry and cathodoluminescence spectroscopy measurements are employed to probe the optoelectronic properties, showing that the band gap decreases with increasing Gd content x and that this effect causes the ideal Gd substitution level for cathodoluminescence applications to be low. Expanding our calculations to other rare earth cations (Pr^{3+} and Tb^{3+}) reveals similar thermodynamic stability and solubility behavior to Gd. From this and previous studies on $Al_{1-x}Sc_xN$, we elucidate that both smaller ionic radius and higher bond ionicity promote increased incorporation of group IIIB cations into wurtzite AlN. This work furthers the development of design rules for new alloys in this material family.

Heterostructural $Al_{1-x}Gd_xN$ Alloys
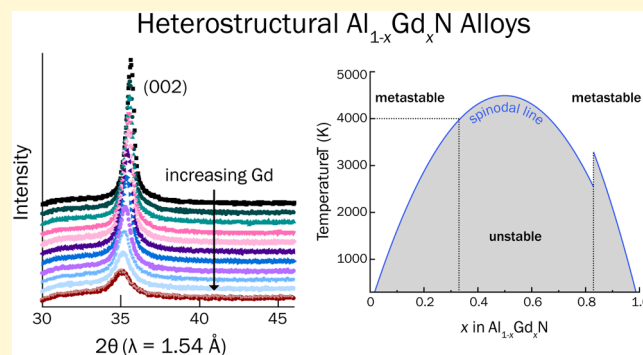
1. INTRODUCTION

Recent joint advances in computational and experimental methods for synthesizing nitride materials have led to a rapid increase in the number of known ternary nitride phases.[1−3] Unlike ordered and stoichiometric compounds, alloys represent a continuous compositional space. Isostructural alloys—solid solutions of two or more materials with the same underlying crystal structure—are the most common types of functional alloys. Isostructural alloys as electronic materials have applications in photovoltaics (e.g., II–VI materials such as $CdSe_xTe_{1-x}$[4] and III–V-based multijunction technologies),[5] energy storage (e.g., $Li_6PS_{5-x}Se_x(Cl,I)$, $Li_3Y_{1-x}In_xCl_3$),[6−8] and thermoelectrics (e.g., $PbSe_xTe_{1-x}$),[9] etc. Heterostructural alloys, in contrast, form between materials with different structures, such as alloys between wurtzite AlN and rocksalt ScN,[10] wurtzite ZnO and rocksalt MnO,[11] and orthorhombic SnS and rocksalt CaS.[12] Beyond their functional properties, they also exhibit interesting thermodynamics of mixing not observed in their isostructural counterparts.[13,14]

Due to their exceptional optoelectronic, charge transport, and electromechanical properties, a large class of polar wurtzite AlN-based alloys is already enabling light-emitting diodes (isostructural $Al_{1-x}Ga_xN$)[15,16] and electromechanical resonators (heterostructural $Al_{1-x}Sc_xN$).[17,18] Scandium-substituted AlN has been the subject of intense interest as a promising new tetrahedral ferroelectric material;[10,19−22] however, the much smaller size of Al^{3+} (~0.39 Å) compared to that of Sc^{3+} (~0.75 Å) presents significant issues for achieving and controlling high Sc incorporation. After significant effort, Sc^{3+} has been substituted into the wurtzite AlN crystal structure at compositions of up to $x \approx 0.43$ (i.e., $Al_{0.57}Sc_{0.43}N$) before phase separation to the rocksalt ScN end-member crystal
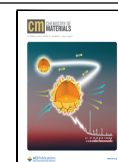
structure occurs.[10,17,23−25] Recent work has shown that the solubility of Sc^{3+} depends both on ionic size and on ionicity, with Sc−N bonds more ionic than Al−N bonds;[24] however, this ionicity effect is difficult to deconvolute from other effects. Other transition-metal cations such as Cr, Zr, Hf, Y, Ta, and Ni have also been investigated as alloys with AlN, and their properties have been studied.[26−30] While it seems unlikely from an ionic radius perspective that any rare earth cations would be able to incorporate into wurtzite AlN, recent work has shown that Er^{3+} and Yb^{3+}, much larger cations than Sc^{3+}, were substituted successfully at $x = 0.015$ and up to $x \approx 0.15$, respectively.[31,33] In GaN, Yb^{3+} can incorporate up to $x \approx 0.3$, consistent with the larger radius of Ga^{3+} (∼0.47 Å).[32]

Incorporating small amounts of Gd^{3+} (∼0.94 Å) into wurtzite AlN and GaN has been investigated primarily for optoelectronic applications such as cathodoluminescence and field-emission devices,[34] given the sharp ultraviolet emission of Gd^{3+} at approximately 320 nm and the AlN host lattice as an established optoelectronic material.[35,36] While most studies utilized ion implantation, direct Gd^{3+} substitution has been attempted with radio-frequency (RF) magnetron sputtering and molecular beam epitaxy (MBE) growth, yielding phase-pure substitution up to $x \approx 0.06$ by sputtering[36,37] and reported incorporation at $x \approx 0.13$ by MBE,[38,39] although it is unclear if a phase-pure wurtzite structure is maintained up to $x \approx 0.13$. In addition to the intriguing optical properties, there are indications that Gd^{3+}-substituted AlN may display interesting and possibly functional magnetic properties.[38,40] In addition to the limited synthesis space, the solubility, stability, and other properties of this alloy material—such as its electrical properties—have been relatively understudied. While ionic size effects are relatively straightforward, other variables that may affect the solubility of large cations in AlN—such as bond ionicity—are underexplored. Given the recent interest in other AlN alloys for electrical and piezoelectric applications, as well as the unique properties of Gd (such as possessing the largest known neutron capture cross section), Gd^{3+}-substituted wurtzite AlN is an appealing material to study for possible functional applications.

We describe here the first synthesis of $Al_{1−x}Gd_xN$ with Gd-cation fraction (x) at least up to ∼0.24 in a confirmed wurtzite structure. We present the results of our joint computational and experimental investigation into the solubility and stability of Gd^{3+} in the AlN wurtzite structure. First-principles calculations of the mixing enthalpy reveal a high critical composition at which the ground state transitions from wurtzite to rocksalt. However, the calculated temperature-composition phase diagram indicates that high (effective) temperatures are needed to incorporate a large amount of Gd^{3+} in a metastabilized wurtzite alloy with AlN. We confirm this experimentally by depositing combinatorial thin films of $Al_{1−x}Gd_xN$ with radio-frequency magnetron cosputtering and performing structural and compositional characterization, as well as optical characterization. Expanding our computational analysis to Pr^{3+} and Tb^{3+} allows us to elucidate the effects that govern the solubility of large 3+ cations in wurtzite AlN.

2. METHODS

2.1. Computational Alloy Modeling. *2.1.1. Structure Relaxation and Electronic Structure.* First-principles calculations were performed with density functional theory (DFT) using the Vienna Ab Initio Simulation Package (VASP) version 5.4.4.[41] The generalized gradient approximation (GGA) of Perdew−Burke−Ernzerhof (PBE) was used as the exchange−correlation functional.[42] The wave functions were expanded as plane waves, and the following projector-augmented wave (PAW) potentials[43] were used to describe the core electrons for $Al_{1−x}Gd_xN$ and related alloys: Al 04Jan2001, N_s 07Sep2000, Gd 23Dec2003, Gd_3 06Sep2000, Tb_3 06Sep2000, and Pr_3 07Sep2000. The Gd_3, Tb_3, and Pr_3 pseudopotentials have the 4f electrons frozen in the core. The DFT-relaxed lattice parameters of wurtzite and rocksalt AlN, GdN, TbN, and PrN are listed in Table S1 of the Supporting Information.

The choice of Gd_3 was motivated by X-ray photoelectron spectroscopy (XPS) studies that have shown that the Gd 4f states in GdN are 7 and 8 eV below the Fermi level[44] and, as such, can be treated as core electrons. To replicate this experimental observation with the Gd pseudopotential (4f electrons treated as valence electrons), an appropriately large on-site Hubbard U correction of +8.0 eV must be applied to the 4f states to avoid artificial hybridization between Gd 4f and N 2p states at the top of the valence band.[45] Figure S2a,b, respectively, show the band structures of GdN computed with Gd pseudopotential without and with the application of U (8.0 eV). Here, the ferromagnetic ordering of Gd magnetic moments was assumed consistent with the experimental ground-state structure.[44,45] Therefore, the Gd_3 pseudopotential, which treats the 4f electrons as core electrons, is expected to provide reasonable results. Furthermore, we found that the polymorph energy difference between the ground-state rocksalt and hypothetical wurtzite phase of GdN with Gd_3 and Gd pseudopotentials ($U = 8.0$ eV, ferromagnetic) is similar (72 vs 70 meV/atom). For completeness, we compared the alloy mixing enthalpy calculated with Gd_3 and Gd (Figure S1) pseudopotentials and found them to have similar alloy interaction parameters and critical composition (x_c) where the wurtzite−rocksalt phase transition occurs. Electronic band structures were calculated on a dense Γ-centered k-point grid determined by $N_{atoms} \times N_{k\text{-points}} \approx 4000$, where N_{atoms} is the number of atoms in the supercell and $N_{k\text{-points}}$ is the number of k-points.

2.1.2. SQS Supercells. Alloys were modeled using special quasirandom structures (SQS).[46] The concept of SQS was developed to mimic completely random alloys without using large supercells or many atomic configurations. An SQS is built through a stochastic search over many possible configurations of local environments within a given supercell to best reproduce the pairwise correlation of a completely random alloy. An optimal SQS is one that minimizes the root-mean-square deviation from the random pairwise correlation. The SQS supercells were constructed using the alloy theoretic automated toolkit (ATAT).[47] We created 108-atom SQS supercells to model the wurtzite phase alloys and 96-atom supercells to model the alloys in the rocksalt phase. For each pseudo-binary alloy, we sampled eight and nine different compositions (x) in addition to the end members to compute the alloy mixing enthalpy. The volumes, cell shapes, and atomic coordinates of the structures were fully relaxed with DFT until the residual forces on each atom were below 0.01 eV/Å. The DFT-relaxed SQS structures are made available in the VASP POSCAR format through a public repository.

2.1.3. Alloy Thermodynamics. The mixing free energy (ΔF_m) is calculated as $\Delta F_m = \Delta H_m - T\Delta S_m$, where ΔS_m is the configurational entropy in the solid solution model and given by $\Delta S_m = -k_B[x \ln(x) + (1 - x)\ln(1 - x)]$. Vibrational contributions to ΔS are neglected, which are typically small compared to the configurational contribution, especially at higher temperatures. ΔH_{mix} is calculated as

$$\Delta H_{mix} = H_{alloy} - \sum_i x_i H_i \tag{1}$$

where H_{alloys} is the enthalpy of the alloy, and x_i and H_i are the composition fraction and enthalpy of each alloy end member in its ground-state structure, i.e., wurtzite AlN and rocksalts GdN, TbN, and PrN. The temperature-composition $T(x)$ phase diagrams are calculated from ΔF_m. The unstable region, which is bounded by the spinodal decomposition line, is computed from the condition $\partial^2 \Delta F_m / \partial^2 x = 0$.

2.2. Thin Film Growth and Characterization. Combinatorial thin films of $Al_{1−x}Gd_xN$ were deposited using RF cosputtering from

elemental targets on 3″ magnetrons in a vacuum sputtering chamber with a base pressure of approximately 5×10^{-7} Torr. The magnetrons were in a standard balanced magnetron configuration, had a working distance of 165 mm, and were at a 120° angle to each other. The PO_2 was $<2 \times 10^{-8}$ Torr, and the PH_2O was $<3 \times 10^{-7}$ Torr at 600 °C The powers used were 340 W (Al, 99.999%) and 120 W (Gd, 99.5%) in a stational substrate geometry, yielding a compositional gradient of $0.12 < x < 0.25$. Deposition occurred at a total chamber pressure of 2 mTorr under 5 sccm of Ar and 15 sccm of N_2 (99.999%) gases (introduced near the targets), and the substrate was heated to T_{sub} = 600 °C. The targets were presputtered for 60 min with the substrate shutter closed, followed by a 60 min deposition with an approximate deposition rate of 3 nm/min. The targets were in a poisoned regime during the growth. Films were grown on 50.8 × 50.8 mm pSi(100) substrates with a native oxide layer (∼3 nm); no substrate pretreatment was performed. Additional homogeneous films were grown at specific compositions by rotating the substrate during deposition.

Experimental combinatorial data for this study have been analyzed using the COMBIgor software package[48] and are publicly available in the National Renewable Energy Laboratory (NREL) high-throughput experimental material database.[49,50] Cation composition was measured with electron probe microanalysis (EPMA) measuring the Al Kα, N Kα, O Kα, Si Kα, and Gd Mα X-ray signals. Extra steps were taken for quantitative analysis of light elements: the sample was fluoresced at different depths using several beam energies (5, 10, and 15 keV), and k-ratios were determined at each. The k-ratios were used to solve iteratively for the film's thickness density as a function of beam energy until a self-consistent composition was obtained for each element. At most points, analytical total compositions summed to slightly less than 1, likely due to impurities from sputter targets. Cation composition was confirmed by X-ray fluorescence (XRF) using a Bruker M4 Tornado under vacuum (∼15 Torr). Thicknesses were extracted from the XRF data following calibration of the model with transmission electron microscopy (TEM).

Laboratory X-ray diffraction (XRD) patterns around the wurtzite (002) peak were collected with Bruker D8 Discover with Cu Kα radiation equipped with a two-dimensional (2D) detector. Additional laboratory XRD data were collected using Cu Kα radiation on a Rigaku Smartlab equipped with parallel beam optics and a Ge(220) monochromator. High-resolution synchrotron grazing incidence wide-angle X-ray scattering (GIWAXS) measurements were performed at beamline 11$\bar{3}$ at the Stanford Synchrotron Radiation Lightsource (SSRL), SLAC National Accelerator Laboratory. The data were collected with a Rayonix 225 area detector at room temperature using a wavelength of λ = 0.9744 Å, a 1° incident angle, a 150 mm sample-to-detector distance, and a spot size of 50 μm × 150 μm. The diffraction images were integrated and processed with GSAS-II, PyFAI, and pygix.[51−53]

Samples were prepared for TEM from each end of the combinatorial film (x = 0.13 and x = 0.24). A cross-sectional sample for TEM and scanning transmission electron microscopy (STEM) with x = 0.13 was prepared using a standard in situ lift-out technique in an FEI Nova NanoLab 200 dual beam focused ion beam (FIB) workstation. A Pt protective layer was deposited first to protect the sample surface during subsequent FIB sample preparation. Ga$^+$ ions (30 kV) were used for most of the preparation, and the samples were finished off using <5 kV Ga$^+$ ions. The FIB damage was subsequently removed in a Fischione NanoMill using <1 kV Ar$^+$ ions with the sample cooled using a liquid nitrogen cold stage. The samples were then examined in an FEI Tecnai F20 UltraTwin field emitting gun (FEG) STEM operated at 200 kV and an FEI Tecnai ST30 TEM operated at 300 kV. Energy-dispersive X-ray spectroscopy (EDS) elemental maps were obtained in the F20 STEM using an EDAX Octane T Optima windowless Si drift detector (SDD) EDS system and processed using EDAX TEAM software. A TEM-ready sample of x = 0.24 was prepared using the ex situ FIB lift-out technique on an FEI Dual Beam FIB/SEM. The samples were capped with carbon-based epoxy/I-C prior to milling. The sample was imaged with an FEI Tecnai Osiris FEG/STEM operated at 200 kV in bright-field (BF)

TEM mode and high-resolution (HR) TEM mode. STEM EDS data were acquired using a Bruker Quantax system.

A rapid thermal annealing (RTA) study was performed on a homogeneous film with x = 0.16 grown at a deposition temperature of 400 °C. Sequential annealing under an 8 slpm flowing N_2 was performed in a ULVAC MILA-3000 RTA furnace at 600, 700, 800, 900, and 1000 °C. The RTA procedure consisted of a 3 min hold at 100 °C and a 1 minute ramp to the set temperature, and a hold at the set temperature for 3 min, followed by rapid cooling to room temperature. Each anneal was followed by laboratory XRD analysis at the (002) peak, as described above.

Spectroscopic ellipsometry data were acquired at 65, 70, and 75° incident angles on a single row of a select sample library (11 points per row; $0.13 < x < 0.24$) and on several homogeneous films (x = 0, 0.03, 0.07, and 0.11) grown on crystalline pSi(100) substrates using a J.A. Woollam Co. M-2000 variable angle ellipsometer. CompleteEASE software (version 6.63) was used to model the data by fitting the real and imaginary parts of the dielectric function with a four-layer model consisting of the silicon substrate, native silicon oxide, the $Al_{1−x}Gd_xN$ film, and surface roughness approximated with a standard mixed film/void Bruggeman EMA layer. The silicon and native oxide were modeled using well-known optical constants provided by the CompleteEASE software. The $Al_{1−x}Gd_xN$ films were modeled using a single parametric semiconductor oscillator (PSemi-M0), which is an established model for accurately fitting the imaginary part of the dielectric function of crystalline semiconductor materials while maintaining the Kramers−Kronig consistency.[54,55]

Cathodoluminescence spectroscopy was performed on a JEOL JSM-7600 FESEM equipped with a Horiba H-CLUE CL system and operating with an accelerating voltage of 5 kV and an incident beam current of ∼5 nA. A grating with 1200 lines/mm and a blaze of 500 nm was used to collect the high-resolution spectra. The presented spectra are the result of averaging five acquisitions of 100 s each, which was done to improve the signal-to-noise ratio.

3. RESULTS AND DISCUSSION

3.1. Thermodynamics of $Al_{1−x}Gd_xN$ Alloys. We calculated the thermodynamics of $Al_{1−x}Gd_xN$ heterostructural alloys using density functional theory (DFT) in conjunction with alloy models (see the Methods section for details). Wurtzite is the ground-state structure for AlN, while GdN is stable in the rocksalt structure. Other lanthanide nitrides such as YbN, LaN, and CeN are also stable in rocksalt ground-state structures. The computed mixing enthalpy (ΔH_m) for $Al_{1−x}Gd_xN$ alloys is shown in Figure 1a. The ΔH_m curves are obtained by fitting second-order polynomials to a set of data points computed at discrete x values. We find that wurtzite is the ground-state structure of $Al_{1−x}Gd_xN$ alloys up to a critical composition of x_c = 0.82, beyond which the ground-state structure is rocksalt. We also considered a layered hexagonal-BN-like structure of the alloys, but we find it to be energetically unfavorable as compared to the wurtzite and rocksalt structures over the full compositional range (Figure S1).

The mixing free energies (ΔF_m) for the wurtzite and rocksalt structures calculated for a range of temperatures (2000−5000 K) are shown in Figure 1b. The temperature-composition $T(x)$ phase diagram shown in Figure 1c is calculated from ΔF_m. The unstable region (gray, shaded) bounded by the spinodal decomposition line is computed from the condition $\partial^2 \Delta F_m / \partial^2 x$ = 0. The shaded region represents the miscibility gap; within this region, single-phase alloys are thermodynamically unstable toward decomposition into AlN and GdN and toward composition fluctuations, i.e., spinodal decomposition. The discontinuity in the spinodal line at x_c is due to the incommensurate lattices of wurtzite and rocksalt, requiring a
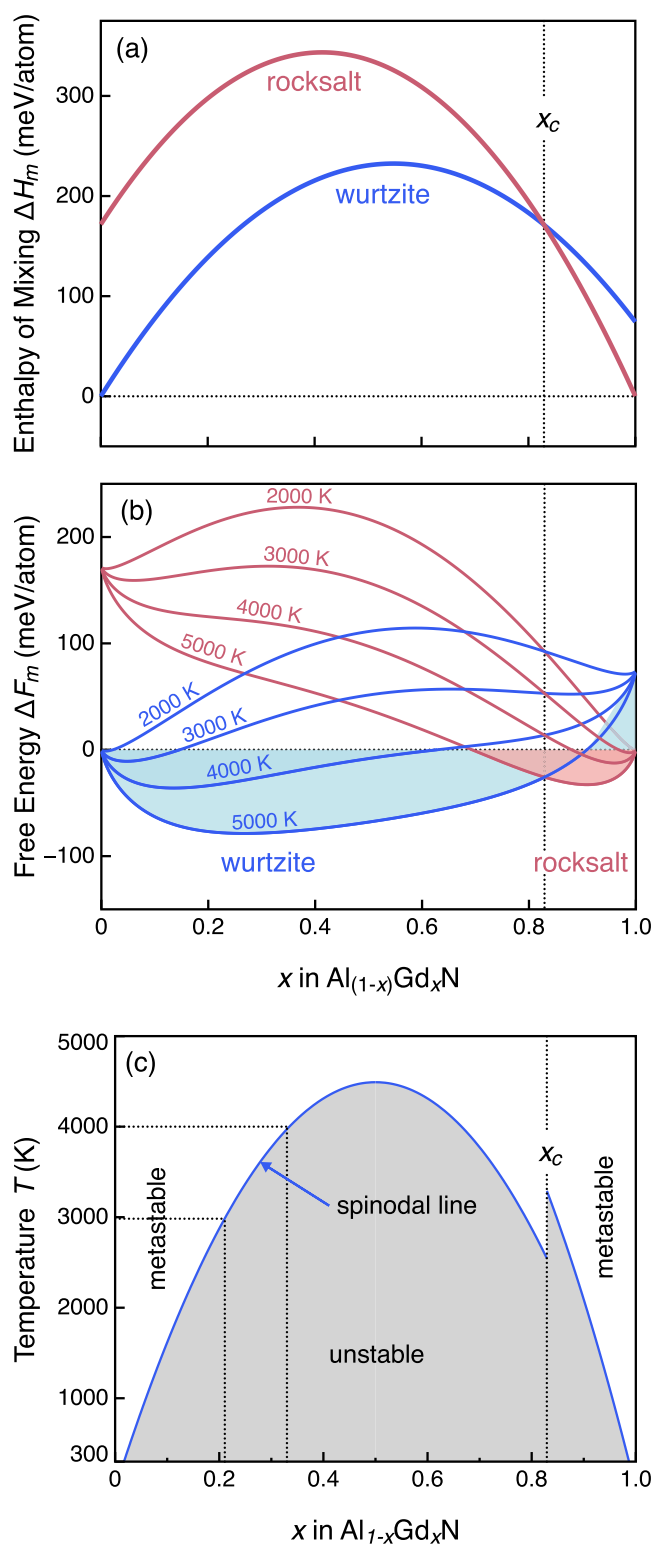
Figure 1. Calculated thermodynamics of heterostructural $Al_{1-x}Gd_xN$ alloys. (a) Mixing enthalpy (ΔH_m) curves of $Al_{1-x}Gd_xN$ alloys in the wurtzite and rocksalt phases. Wurtzite is the ground-state structure of AlN and $Al_{1-x}Gd_xN$ alloys up to the critical composition of $x_c = 0.82$, above which the rocksalt structure is more stable. (b) Free energy (ΔF_m) calculated for a range of temperatures $T = 2000-5000$ K. (c) Temperature (T)-composition phase diagram showing the miscibility gap bounded by the spinodal lines for the wurtzite ($x_c \leq 0.82$) and rocksalt ($x_c \geq 0.82$) alloys. A region of metastability exists immediately beyond the unstable region.

reconstructive phase transition. Beyond the unstable region is a region where single-phase alloys are metastable. The metastable region extends up to the binodal line, which can be obtained through the common tangent construction to ΔF_m curves (not shown in Figure 1c). Above the binodal line, single-phase alloys are miscible and stable under thermodynamic equilibrium. We restrict our discussion to the unstable and metastable regions because accessible experimental conditions most likely fall within these regions when considering effective temperatures (see the discussion below).

The large miscibility gap in the $T(x)$ phase diagram at low temperatures ($T < 1000$ K) suggests that only small amounts of Gd can be alloyed with AlN under equilibrium conditions. Therefore, the key to synthesizing Gd-rich wurtzite $Al_{1-x}Gd_xN$ alloys is by accessing high (effective) temperatures under nonequilibrium conditions. Material growth techniques involving highly energetic species such as sputtering, plasma-assisted growth, etc., can create nonequilibrium conditions with extremely high local effective temperatures.[56] Such nonequilibrium growth techniques have been previously demonstrated, resulting in the synthesis of isostructural and heterostructural alloys at compositions deep inside the miscibility gap. Successful synthesis of $Mn_{1-x}Zn_xO$,[11] $Sn_{1-x}Ca_xS$,[12] and $Al_{1-x}Sc_xN$[10] suggests that the effective temperatures in nonequilibrium growth are much higher than suggested by equilibrium conditions. In the case of $Al_{1-x}Gd_xN$, we find that effective temperatures of 3000 and 4000 K can stabilize alloy compositions with $x > 0.2$ and $x > 0.3$, respectively, in a metastable state (see Figure 1c).

There are several parameters, including substrate temperature and kinetic barriers for decomposition, that govern metastable phase formation. Without minimizing the importance of each of these parameters, we invoke the concept of an emergent effective temperature T_{eff} (above), in the same spirit as previously proposed for heterostructural alloys, colloidal particle segregation,[57] granular materials,[58] and turbulent fluids.[59] By defining an emergent T_{eff} one is able to extend the framework and profound insights into (equilibrium) statistical thermodynamics to nonequilibrium systems.[57] Due to its dependence on multiple parameters, precise control of T_{eff} is challenging.

3.2. Thin Film Growth, Composition, and Structure. Using RF cosputtering of metallic targets in a mixed N_2/Ar gas environment, we have grown thin film combinatorial samples of $Al_{1-x}Gd_xN_y$ with a 1-dimensional compositional gradient on pSi(100) substrates. The films grown and characterized here are ~140–200 nm thick (see Figure 4a,d). We tuned the growth conditions to achieve crystalline films with high Gd contents (x). Process variables that were tuned included the magnetron powers (to achieve the desired compositional gradient), the process pressure, the N_2/Ar ratio, and the substrate temperature (T_{sub}) from ambient to 800 °C. For substrate temperatures above 600 °C, the wurtzite phase is (meta)stabilized with a wider range of Gd incorporation up to $x = 0.24$. The Gd and Al target power ratio was set between 1:3 and 1:1 to achieve a range of Gd content (0.13–0.52). The total power density was found to be an insignificant variable for phase stability. Higher N_2/Ar ratios (15/5 sccm) were found to increase crystallinity without detrimental effects on Gd incorporation. Process pressures ranging from 2 to 20 mTorr did not remarkably affect the wurtzite phase stability, but 2 mTorr was employed to encourage higher deposition rates.
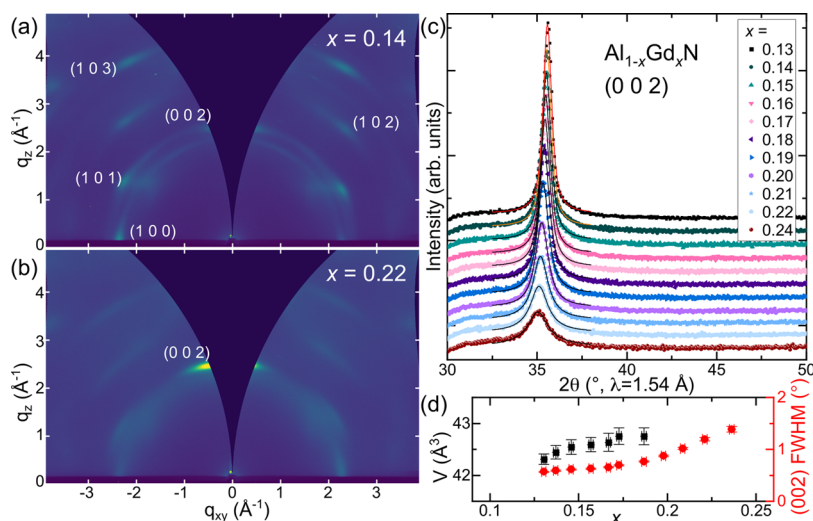
Figure 2. Synchrotron GIWAXS 2D detector images of spots along the compositional gradient of an $Al_{1-x}Gd_xN$ film for (a) $x = 0.14$ and (b) $x = 0.22$. (c) Laboratory XRD at the wurtzite (002) peak across the combinatorial film; lines are pseudo-Voigt fits. (d) Unit cell volume V and 2θ FWHM of the (002) peak as a function of x, derived from fitting the wurtzite (002) and (102) peaks (see Figure S3 in the Supporting Information for the (102) peak data). The error bars are derived from the fits; to account for the ~10% combinatorial gradient over 40 mm, we included 0.25% error bars in x.
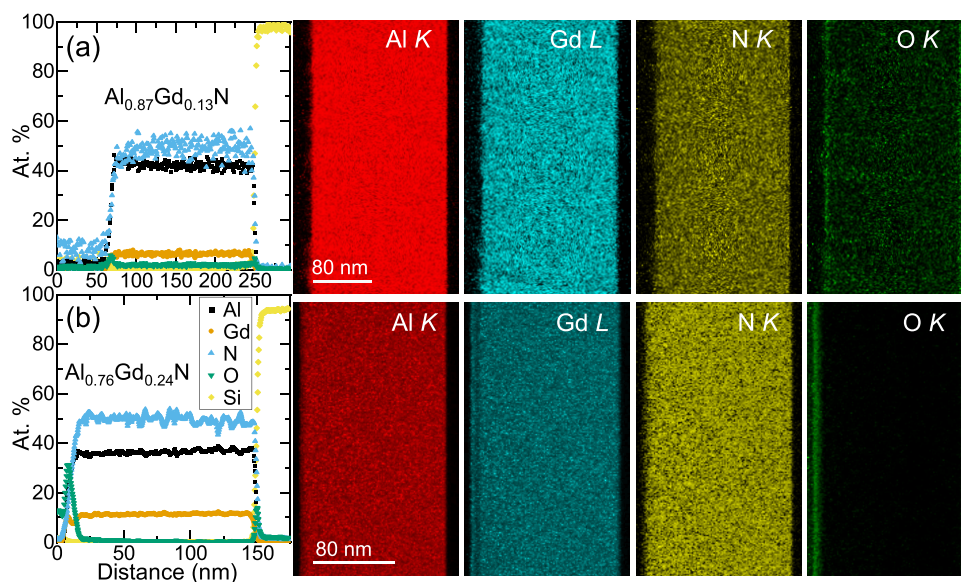

Figure 3. EDS atomic % line profiles and elemental mapping at the Al K-peak, Gd L-peak, N K-peak, and O K-peak for regions of the combinatorial films with (a) $x \approx 0.13$ and (b) $x \approx 0.24$. The line profiles were extracted from the EDS maps, and the values have been calibrated with the chemical formulas measured via EPMA. Pt, C, and F are not shown in the line profiles. Additional elemental maps are shown in Figures S6 and S7.

The growths were additionally reproduced in a second sputtering chamber, yielding similar results.

The cation (Al/Gd) ratio was characterized by electron probe microanalysis (EPMA), yielding a compositional gradient of $0.12 < x < 0.25$ across a 50.8 mm combinatorial sample grown at $T_{sub} = 600$ °C. Consistency checks were performed with X-ray fluorescence (XRF), Rutherford back-scattering spectrometry, and Auger electron spectroscopy. EPMA also probes the anion content, revealing a low amount of oxygen incorporation. The average N/O ratio across the combinatorial film is 96:4 atomic % (i.e., $Al_{0.87}Gd_{0.13}N_{0.96}O_{0.04}$ to $Al_{0.76}Gd_{0.24}N_{0.95}O_{0.05}$), consistent with the higher oxophilicity of Gd compared to that of Al. This level of oxygen incorporation is typical for a new nitride material grown by

sputtering,[2,60,61] and while it may affect the optoelectronic properties, it should not affect the crystal structure.

Using high-resolution synchrotron grazing incidence wide-angle X-ray scattering (GIWAXS) data collected at SSRL beamline 11-$\overline{3}$ (Figure 2a,b), we observe that a wurtzite structure is maintained up to a substitution value of $x \approx 0.24$. No peaks arising from metallic Gd or rocksalt structure GdN are observed. The 2D detector images display texturing consistent with a semioriented sample, and the texturing grows less pronounced at higher x values (see Figure 2a,b). The successful substitution of Gd is confirmed by the increase in unit cell volume shown in Figure 2d; the trend is close to Vegard's law, implying a continuous solid solution in this substitution region. The full width at half-maximum (FWHM) of the peak in 2θ increases with increasing Gd x, suggesting
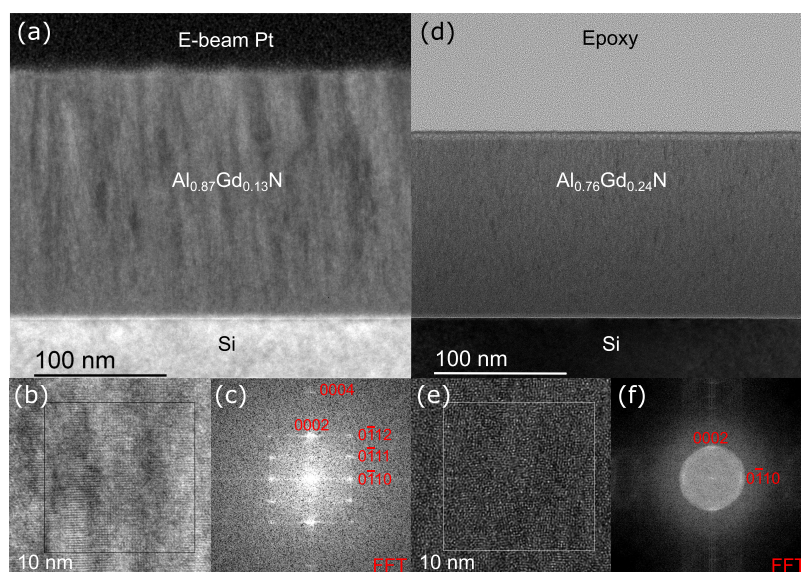
Figure 4. (a–c) TEM on a region of the combinatorial film with $x \approx 0.13$. (d–f) TEM on a region of the combinatorial film with $x \approx 0.24$. (a, d) BF TEM image taken along a $\langle 110 \rangle$ Si direction, (b, e) HRTEM taken along a $\langle 2\bar{1}\bar{1}0 \rangle$ $Al_{1-x}Gd_xN$ direction, and (c, f) the fast Fourier transform (FFT) of the boxed area in panel (b) showing periodicities corresponding to the $\langle 2\bar{1}\bar{1}0 \rangle$ zone axis of the wurtzite crystal structure of $Al_{1-x}Gd_xN$. The zone axis periodicities were calculated in CrystalMaker.[63]

that the film becomes increasingly nanocrystalline. Lattice parameters c and a were extracted from pseudo-Voigt fits of laboratory X-ray diffraction (XRD) data collected at the (002) and (102) peaks with a 2D detector (Figures 2c and S3 in the Supporting Information). c, a, and the c/a ratios are plotted in Figure S3 in the Supporting Information. Additional fits performed on higher-resolution XRD data collected with a point detector on the (002) peak of the combinatorial film and several single composition films are shown in Figure S4; they confirm the increase in c with increasing Gd x.

The thermal stability of $Al_{1-x}Gd_xN$ was investigated via a sequential rapid thermal annealing study performed in a flowing N_2 on a film with $x \approx 0.16$ grown at 400 °C (see Figure S5 in the Supporting Information). No decomposition, for example, to metallic Gd or rocksalt GdN, was observed via laboratory XRD as a result of sequential 3 min anneals every 100 from 600 °C up to 1000 °C. There is no significant change in the unit cell volume across the temperature range, as shown in Figure S5c, so we attribute small shifts in the (002) peak position to strain effects from mismatch in the coefficients of thermal expansion between $Al_{1-x}Gd_xN$ and the Si substrate.

The phase-pure substitution level attained here by RF sputtering ($x \approx 0.25$) is significantly higher than that achieved previously by either RF sputtering ($x \approx 0.06$)[36,62] or molecular beam epitaxy ($x = 0.13$).[38,39] Kita et al. observed phase separation to metallic Gd and AlN above $x \approx 0.1$ grown at 500 °C by RF sputtering,[36] which we do not observe in Figures 2 or S3 and S4. We attribute the higher substitution level at which we observe phase-pure wurtzite compared to previous reports to different deposition conditions. We have previously extensively optimized for nonequilibrium growth conditions (i.e., deposition temperature, process pressure, gas ratios) based on our past experience with related $Al_{1-x}M_xN$ alloys.[10,19−21,24] We expect that additional optimization of growth parameters may be able to further increase the amount of Gd^{3+} that can be incorporated into AlN.

STEM energy-dispersive X-ray spectroscopy (EDS) elemental mapping using the Al, N, and O K-peaks and the Gd L-

peak with approximately 1 nm spatial resolution for regions of the combinatorial film with $x \approx 0.13$ and $x \approx 0.24$ is shown in Figure 3, with additional elemental maps in Figures S6 and S7. The EDS maps indicate the homogeneous incorporation of Al, Gd, and N within the film for both $x \approx 0.13$ and $x \approx 0.24$. Consistent with the EPMA results, there is a low amount of oxygen throughout the film, with thin surface oxide layers visible between the film and the Si substrate (due to the native oxide on the substrate) as well as at the top of the film layer. Atomic % line profiles extracted from the EDS maps confirm the compositional homogeneity through each film region and the low amount of oxygen present in the bulk of the film. The homogeneous distribution confirms the successful growth of a single-phase film of $Al_{1-x}Gd_xN$ with x at least up to 0.24. We experimentally achieved the highest Gd solubility yet reported (up to $x \approx 0.24$) in kinetically limited thin film growth at T_{sub} = 600 °C; this level could be achieved only at approximately T = 3300 K on the calculated bulk thermodynamic phase diagram (Figure 1c). This is likely due to the high energy (tens of eV, depending on sputtering conditions and chamber geometry; kT of which would correspond to ≫4000 K) of the impending species during the sputtering, part of which is transferred to the adsorbed atoms on a growing film surface.

Both regions of the combinatorial film, with $x \approx 0.13$ and $x \approx 0.24$, were further investigated with TEM, shown in Figures 4 and S8 and S9 in the Supporting Information. A bright-field (BF) TEM image of the $x \approx 0.13$ film (Figure 4a) displays a polycrystalline film with columnar grains, typical for sputtered films and consistent with the semioriented nature of the GIWAXS patterns. BF TEM imaging of the $x \approx 0.24$ film (Figure 4d) reveals a more uniform film; slight amounts of surface damage may be due to amorphization or oxidation. High-resolution TEM (HRTEM) imaging of both composition regions is consistent with a wurtzite structure based on fast Fourier transform (FFT) analyses (Figure 4b,c,e,f). The FFTs are labeled according to a single-crystal electron diffraction pattern calculated for the $\langle 2\bar{1}\bar{1}0 \rangle$ zone of the wurtzite crystal structure; such a pattern would not be observed for a cubic

crystal structure. No indications of cubic rocksalt or zincblende structures were found. Additionally, selected area electron diffraction (SAED) patterns for the $x \approx 0.13$ and $x \approx 0.24$ regions (shown in Figure S8) confirm the wurtzite structure and indicate that the film is textured, consistent with the GIWAXS and XRD data. It is possible that there could be some regions of amorphous $Al_{1-x}Gd_xN$ in the high-Gd ($x \approx 0.24$) end of the combinatorial film. However, as the region of interest for the $x \approx 0.24$ SAED (Figure S8d) included the epoxy, it is not possible to distinguish whether the amorphous background in Figure 4f is due to epoxy or from $Al_{1-x}Gd_xN$. Using the Si pattern as a reference, the d-spacing of the labeled {002} $Al_{1-x}Gd_xN$ reflection in the $x \approx 0.13$ SAED (Figure S8b) is calculated to be ~2.51 Å, indicating $c \approx 5.02$ Å, which is consistent with the XRD results (see Figures 2d, S3, and S4).

To probe the optical and electronic properties of these films, which have been the primary focus of previous studies of this material family, cathodoluminescence spectroscopy (CL) and spectroscopic ellipsometry measurements were performed across the combinatorial sample, as well as on several homogeneous films with lower Gd x values. The absorption coefficients (α) extracted from modeling the ellipsometry data are displayed in Figure 5a. Instead of defining a band gap (E_g) using Tauc analysis, which can be fraught with error due to assumptions about the gap nature (direct vs indirect) and linear fit region, we define an optical absorption onset as the energy when $\alpha = 10^4$ cm^{-1}. This is shown in Figure 5b, and we attribute the shift toward lower energy with higher Gd content to the fundamental band gap decreasing. Although this analysis does not yield the absolute E_g, the trend is consistent with the values extracted from a preliminary Tauc analysis. The band gaps extracted from DFT calculations are plotted on the right axis of Figure 5b. Both show a decreasing trend; however, the calculated band gaps do not plateau at higher x values, as is observed in the absorption onset trend. The calculated band gaps decrease almost linearly with x; a linear dependence is typically observed in many binary semiconductor isostructural alloys. We note that the calculated band gaps are severely underestimated by DFT; therefore, only qualitative trends can be extracted. We speculate that the plateau in the absorption onset is likely due to defects in the sputtered films—such as the small level of oxygen incorporation—as well as strain effects in the combinatorial sample and the choice of α cutoff; these effects are not captured in the calculations.

The sharp CL emission at ~3.90 eV associated with the internal transition of Gd^{3+} in $Al_{1-x}Gd_xN$ has been investigated for ultraviolet (UV) emission applications such as field-emission devices, with a focus on low Gd content (x).[36,62,64] The highest Gd concentration measured (or synthesized) previously is $x = 0.13$, grown via MBE; Choi et al. found that the CL signal of this $x = 0.13$ sample was suppressed compared to a sample with $x = 0.02$, attributing this behavior to concentration quenching.[65] To investigate the interplay between Gd incorporation and its effects on band gap and CL intensity, we measured CL spectra on several homogeneous films with a wide range of Gd x values, from $x = 0$ (i.e., AlN) to $x = 0.16$. The spectra, in Figure 5c, show a sharp peak at 3.90 eV (318 nm) for the samples with $x > 0$, consistent with previous reports that assigned this peak to the radiative transition of Gd^{3+} from its first excited state ($^6P_{7/2}$) to its ground state ($^8S_{7/2}$).[35,66] The shoulder at ~3.97 eV (312 nm) is likely due to the $^6P_{5/2}$ to $^8S_{7/2}$ transition and phonon replicas of the main transition.[35,65] We find the highest intensity of the
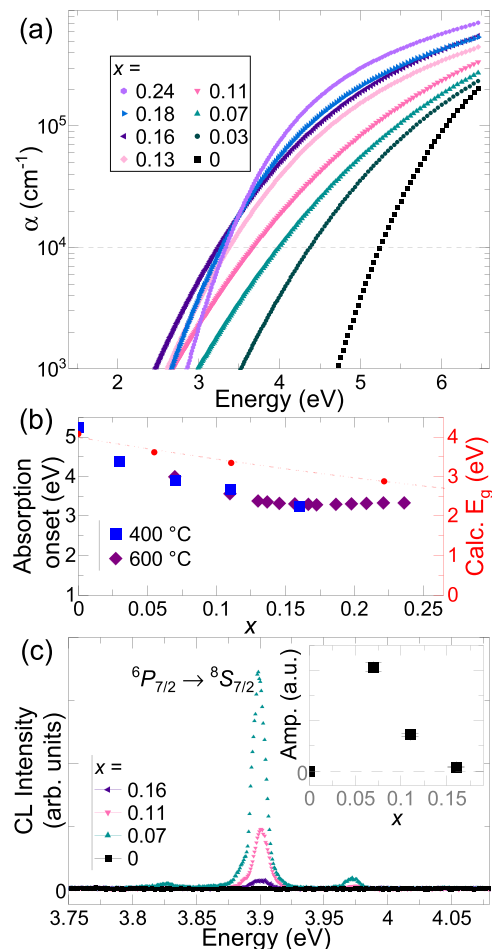

Figure 5. (a) Absorption coefficient α extracted from spectroscopic ellipsometry data of the combinatorial sample and several single composition films. (b) The absorption onset as a function of Gd content x of the combinatorial film (grown at $T_{sub} = 600$ °C) and several single composition films grown at $T_{sub} = 400$ °C. The absorption onset is calculated as the energy at which each curve intersects with $\alpha = 10^4$ cm^{-1} (see the dashed line in panel a). The calculated band gaps (E_g) extracted from DFT are shown on the right axis; the line is a quadratic fit to the data. (c) CL data for several single composition films grown at $T_{sub} = 400$ °C with similar thicknesses. The inset displays the amplitude of the main luminescence at 3.899 eV (318 nm) extracted from pseudo-Voigt fits.

3.90 eV peak at $x = 0.07$, with a significant decrease for higher Gd incorporation. A sample with $x = 0.03$ was also measured and showed significantly higher intensity but cannot be compared quantitatively due to a different thickness. The decrease in CL intensity at $x > 0.07$ is likely due to a combination of concentration quenching as well as the increased absorption of the emitted light due to the concentration dependence of the absorption coefficient of the host material, as the band gap shifts to lower energy with increasing Gd substitution (Figure 5a,b). These trends imply that the optimal Gd incorporation for emission-focused applications is low, certainly below $x \approx 0.1$. Further synthetic optimization of our growth parameters will likely be required to further increase the CL emission by decreasing defects such as substitutional oxygen and decreasing sub-band-gap absorption.

3.3. Thermodynamics of Other $Al_{1-x}M_xN$ Alloys. Given the widespread interest in $Al_{1-x}M_xN$-based (M: group-3
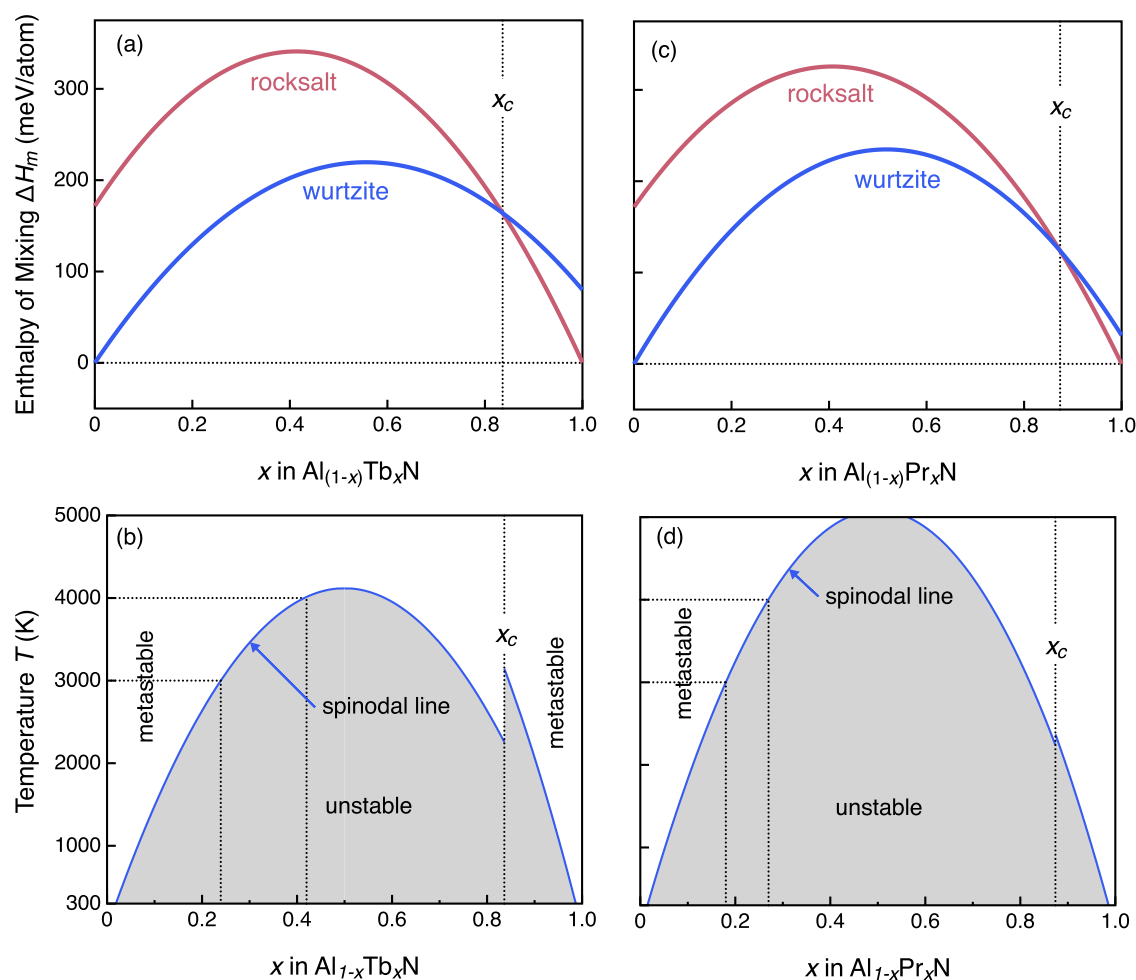
Figure 6. (a, c) Calculated mixing enthalpy (ΔH_m) curves of $Al_{1-x}Tb_xN$ and $Al_{1-x}Pr_xN$ alloys in the wurtzite and rocksalt phases. The critical compositions above which the rocksalt structure is more stable are $x_c = 0.84$ (Tb) and $x_c = 0.87$ (Pr). (b, d) Temperature (T)-composition phase diagrams of $Al_{1-x}Tb_xN$ and $Al_{1-x}Pr_xN$ alloys showing the miscibility gap bounded by the spinodal lines for the wurtzite and rocksalt alloys.

transition metal or rare earths) alloys, and motivated by our success in realizing Gd-rich $Al_{1-x}Gd_xN$, we computationally investigated the formation thermodynamics of related alloys. The goal here is to (1) assess whether M-rich heterostructural $Al_{1-x}M_xN$ alloys can be (*meta*)stabilized using similar non-equilibrium thin film growth used for $Al_{1-x}Gd_xN$ and (2) derive trends across the series of $Al_{1-x}M_xN$ alloys and formulate design principles. Figure 6 shows the calculated formation thermodynamics of $Al_{1-x}Tb_xN$ and $Al_{1-x}Pr_xN$ alloys. For consistency, the same DFT methodology as used for $Al_{1-x}Gd_xN$ alloy calculations is adopted for the Tb and Pr analogues. Here, Tb is chosen because of its similar ionic size and electronegativity to Gd and Pr because it lies in the lanthanoid series between La (no f electrons) and Gd.

The critical compositions (x_c) for wurtzite → rocksalt phase transition in the three $Al_{1-x}M_xN$ alloy systems studied here are 0.82 (M = Gd), 0.84 (M = Tb), and 0.87 (M = Pr). Previous computational studies have predicted x_c for other AlN alloys with group-3 binary nitrides, shown in Table 1. We observe a nonmonotonic change in x_c as we move down group-3 and across the lanthanide series, with x_c first increasing from Sc → La and then decreasing through to Yb. The trend is counterintuitive if one considers only the changes in the ionic size. The M^{3+} cation sizes in octahedral coordination, which is the native coordination in the ground-state MN

Table 1. Ionic Radius (in Å), Electronegativity (χ, Pauling Scale), and Calculated Critical Composition (x_c) for Several Group-3 Cations Investigated for Incorporation into Wurtzite AlN in This Work and Previous Studies[a][67]

cation	ionic radius	χ	x_c	ref
Sc^{3+}	0.75	1.36	0.55–0.64	10, 29
Y^{3+}	0.90	1.22	0.75	29
La^{3+}	1.03	1.10	0.95	68
Pr^{3+}	0.99	1.13	0.87	this work
Gd^{3+}	0.94	1.20	0.82	this work
Tb^{3+}	0.92	1.10	0.84	this work
Yb^{3+}	0.87	1.10	0.75	32
Al^{3+}	0.39	1.61		

[a]The radii are from Shannon in octahedral coordination, which is the native coordination in the ground-state MN rocksalt phase.[67]

rocksalt phase, are tabulated in Table 1. Here, the systematic decrease in the ionic radii beyond La is due to the well-known "lanthanide contraction." La has the largest ionic size mismatch with Al, and therefore we would expect the transition to the rocksalt phase to occur at the smallest x_c. However, this is not the case ($x_c = 0.95$),[68] which indicates that the ionic size mismatch is not the primary factor.

The nonmonotonic change in x_c is likely driven by the ionicity of $M-N$ bonds. Sc is the most electronegative (1.36 on the Pauling scale) and La is the least (1.10). The electronegativity of rare earth elements increases from La → Yb. Al–N bonds have a strong polar-covalent character owing to the high electronegativity (1.61) of Al. $M-N$ bonds are relatively more ionic, with La–N bonds expected to be the most ionic based on electronegativities. As discussed in the context of $Al_{1-x}Sc_xN$ alloys,[24] the polar-covalent Al–N bonds composed of sp^3-hybridized orbitals are highly directional. In comparison, more ionic $M-N$ bonds tend to be spherically symmetric and nondirectional, which may allow easier incorporation in the Al–N matrix. As such, a large x_c is predicted for $Al_{1-x}La_xN$ alloys.[68]

We have demonstrated in this work that Gd-rich $Al_{1-x}Gd_xN$ compositions can be metastabilized with highly nonequilibrium thin film growth techniques. From Figure 1c, we find that effective temperatures of 3000–4000 K are needed to metastabilize $Al_{1-x}Gd_xN$ compositions with $x > 0.3$. Such high effective temperatures can be achieved only with nonequilibrium growth, e.g., by bombardment of highly energetic atoms/ions (sputtering). Since the solubility of group-3 element M in the wurtzite AlN phase is temperature-dependent, we use 4000 K as the reference T to compare the predictions between different alloys. Like Gd, we find that Tb and Pr exhibit relatively high solubilities in wurtzite AlN, with $x = 0.42$ and $x = 0.28$ achieved at $T = 4000$ K, respectively (Figure 6b,d). In comparison, other studies have computationally predicted $x = 0.25$ for $Al_{1-x}Sc_xN$[10] and $x = 0.1-0.15$ for $Al_{1-x}Yb_xN$[69] at $T = 4000$ K. It is not clear why Yb solubility is significantly lower compared to other group-3 elements.[32,69] From a DFT calculation perspective, Yb is a particularly challenging f-electron element that exhibits mixed valence (Yb^{2+}, Yb^{3+}); Yb_3 pseudopotential is not available with VASP distribution, and Yb_2 is a valid choice only when Yb exists predominantly as Yb^{2+}, which is not the case in $Al_{1-x}Yb_xN$. The use of the Yb pseudopotential, where the 4f electrons are treated as valence electrons, requires careful consideration of the magnetic ordering. We can conclude that a large family of M-rich wurtzite $Al_{1-x}M_xN$ heterostructural alloys can be realized at effective T that can be accessed with nonequilibrium growth techniques such as sputtering.

4. CONCLUSIONS

Heterostructural alloys of wurtzite AlN and rocksalt MN are promising materials for a host of applications, including optoelectronic, ferroelectric, and neutron detection, among others. A fundamental understanding of the thermodynamics of alloy stability, phase transition, and solubility of M cations is, therefore, central to designing and optimizing $Al_{1-x}M_xN$ alloys. We have performed a joint computational and experimental study on the incorporation of Gd^{3+} into AlN, creating a heterostructural alloy $Al_{1-x}Gd_xN$ between rocksalt GdN and wurtzite AlN. First-principles calculations using density functional theory in conjunction with SQS supercells reveal that the critical composition for a wurtzite to rocksalt phase transition is $x_c = 0.82$. The calculated mixing free energy indicates that at equilibrium conditions and at temperatures below 1000 K, there is a large miscibility gap and only a few percent of Gd can be incorporated in AlN. Higher (effective) temperatures that can be accessed with nonequilibrium growth methods will enable higher Gd incorporation. By exploiting these nonequilibrium growth conditions experimentally via combinatorial RF cosputtering, we have achieved significantly higher Gd concentrations in the wurtzite phase ($x \approx 0.25$) than in previous thin film syntheses and therefore significantly expanded the range of alloys in this new material system. Future growth optimization may be able to further increase the range of Gd that can be incorporated into AlN. Expanding our computational analysis to Pr^{3+} and Tb^{3+}, which show similar behavior to Gd^{3+}, and comparing ionic size effects with electronegativity for all of the cations that have been considered for substitution into AlN allows us to develop design rules for $Al_{1-x}M_xN$ alloys. We find that increased ionicity of the $M-N$ bond aids in the substitution of larger M cations into wurtzite AlN, in which the Al–N bond is highly polar and covalent. The combination of higher bond ionicity and experimental access to nonequilibrium growth conditions provides a path forward for designing other heterostructural alloys within this family.

■ ASSOCIATED CONTENT

Ⓢ Supporting Information

The Supporting Information is available free of charge at https://pubs.acs.org/doi/10.1021/acs.chemmater.2c02783.

> Calculated mixing enthalpy of $Al_{1-x}M_xN$ alloys; the electronic structure of GdN; DFT-calculated lattice parameters; additional X-ray diffraction data; data supporting the thermal stability of $Al_{1-x}M_xN$ alloys; and additional transmission electron microscopy data (PDF)

■ AUTHOR INFORMATION

Corresponding Authors

Rebecca W. Smaha − National Renewable Energy Lab, Golden, Colorado 80401, United States; ⓞ orcid.org/0000-0002-8349-2615; Email: rebecca.smaha@nrel.gov

Prashun Gorai − Colorado School of Mines, Golden, Colorado 80401, United States; National Renewable Energy Lab, Golden, Colorado 80401, United States; Email: pgorai@mines.edu

Nancy M. Haegel − National Renewable Energy Lab, Golden, Colorado 80401, United States; Email: nancy.haegel@nrel.gov

Authors

Keisuke Yazawa − National Renewable Energy Lab, Golden, Colorado 80401, United States

Andrew G. Norman − National Renewable Energy Lab, Golden, Colorado 80401, United States; ⓞ orcid.org/0000-0001-6368-521X

John S. Mangum − National Renewable Energy Lab, Golden, Colorado 80401, United States; ⓞ orcid.org/0000-0002-5926-7565

Harvey Guthrey − National Renewable Energy Lab, Golden, Colorado 80401, United States; ⓞ orcid.org/0000-0003-1574-3379

Geoff L. Brennecka − Colorado School of Mines, Golden, Colorado 80401, United States; ⓞ orcid.org/0000-0002-4476-7655

Andriy Zakutayev − National Renewable Energy Lab, Golden, Colorado 80401, United States; ⓞ orcid.org/0000-0002-3054-5525

Sage R. Bauers − *National Renewable Energy Lab, Golden, Colorado 80401, United States;* ⊙ orcid.org/0000-0002-6505-5016

Complete contact information is available at:
https://pubs.acs.org/10.1021/acs.chemmater.2c02783

Author Contributions

§R.W.S. and K.Y. contributed equally to this work.

Notes

The authors declare no competing financial interest.
The DFT-relaxed SQS structures used for modeling the alloys are available on GitHub (https://github.com/prashungorai/papers/tree/main/2022/algdn_alloy). Experimental data are publicly available in the National Renewable Energy Laboratory (NREL) high-throughput experimental materials database (https://htem.nrel.gov).

■ REFERENCES

(1) Sun, W.; Bartel, C. J.; Arca, E.; Bauers, S. R.; Matthews, B.; Orvañanos, B.; Chen, B. R.; Toney, M. F.; Schelhas, L. T.; Tumas, W.; Tate, J.; Zakutayev, A.; Lany, S.; Holder, A. M.; Ceder, G. A map of the inorganic ternary metal nitrides. *Nat. Mater.* **2019**, *18*, 732−739.

(2) Bauers, S. R.; Holder, A.; Sun, W.; Melamed, C. L.; Woods-Robinson, R.; Mangum, J.; Perkins, J.; Tumas, W.; Gorman, B.; Tamboli, A.; Ceder, G.; Lany, S.; Zakutayev, A. Ternary nitride semiconductors in the rocksalt crystal structure. *Proc. Natl. Acad. Sci. U.S.A.* **2019**, *116*, 14829−14834.

(3) Zakutayev, A.; Bauers, S. R.; Lany, S. Experimental Synthesis of Theoretically Predicted Multivalent Ternary Nitride Materials. *Chem. Mater.* **2022**, *34*, 1418−1438.

(4) Metzger, W. K.; Grover, S.; Lu, D.; Colegrove, E.; Moseley, J.; Perkins, C. L.; Li, X.; Mallick, R.; Zhang, W.; Malik, R.; et al. Exceeding 20% efficiency with in situ group V doping in polycrystalline CdTe solar cells. *Nat. Energy* **2019**, *4*, 837−845.

(5) Geisz, J. F.; France, R. M.; Schulte, K. L.; Steiner, M. A.; Norman, A. G.; Guthrey, H. L.; Young, M. R.; Song, T.; Moriarty, T. Six-junction III−V solar cells with 47.1% conversion efficiency under 143 Suns concentration. *Nat. Energy* **2020**, *5*, 326−335.

(6) Bernges, T.; Culver, S. P.; Minafra, N.; Koerver, R.; Zeier, W. G. Competing Structural Influences in the Li Superionic Conducting Argyrodites $Li_6PS_{5-x}Se_xBr$ ($0 \leq x \leq 1$) upon Se Substitution. *Inorg. Chem.* **2018**, *57*, 13920−13928.

(7) Schlem, R.; Ghidiu, M.; Culver, S. P.; Hansen, A.-L.; Zeier, W. G. Changing the Static and Dynamic Lattice Effects for the Improvement of the Ionic Transport Properties within the Argyrodite $Li_6PS_{5-x}Se_xI$. *ACS Appl. Energy Mater.* **2020**, *3*, 9−18.

(8) Combs, S. R.; Todd, P. K.; Gorai, P.; Maughan, A. E. Editors' Choice—Review—Designing Defects and Diffusion through Substitutions in Metal Halide Solid Electrolytes. *J. Electrochem. Soc.* **2022**, *169*, 40551.

(9) Tian, Z.; Garg, J.; Esfarjani, K.; Shiga, T.; Shiomi, J.; Chen, G. Phonon conduction in PbSe, PbTe, and $PbTe_{1-x}Se_x$ from first-principles calculations. *Phys. Rev. B* **2012**, *85*, 184303.

(10) Talley, K. R.; Millican, S. L.; Mangum, J.; Siol, S.; Musgrave, C. B.; Gorman, B.; Holder, A. M.; Zakutayev, A.; Brennecka, G. L. Implications of heterostructural alloying for enhanced piezoelectric performance of (Al,Sc)N. *Phys. Rev. Mater.* **2018**, *2*, 063802.

(11) Peng, H.; Ndione, P. F.; Ginley, D. S.; Zakutayev, A.; Lany, S. Design of Semiconducting Tetrahedral $Mn_{1-x}Zn_xO$ Alloys and Their Application to Solar Water Splitting. *Phys. Rev. X* **2015**, *5*, 021016.

(12) Vidal, J.; Lany, S.; Francis, J.; Kokenyesi, R.; Tate, J. Structural and electronic modification of photovoltaic SnS by alloying. *J. Appl. Phys.* **2014**, *115*, 113507.

(13) Holder, A. M.; Siol, S.; Ndione, P. F. Novel phase diagram behavior and materials design in heterostructural semiconductor alloys. *Sci. Adv.* **2017**, *3*, e1700270.

(14) Siol, S.; Holder, A.; Steffes, J.; Schelhas, L. T.; Stone, K. H.; Garten, L.; Perkins, J. D.; Parilla, P. A.; Toney, M. F.; Huey, B. D.; Tumas, W.; Lany, S.; Zakutayev, A. Negative-pressure polymorphs made by heterostructural alloying. *Sci. Adv.* **2018**, *4*, eaaq1442.

(15) Ponce, F. A.; Bour, D. P. Nitride-based semiconductors for blue and green light-emitting devices. *Nature* **1997**, *386*, 351−359.

(16) Nakamura, S. The Roles of Structural Imperfections in InGaN-Based Blue Light-Emitting Diodes and Laser Diodes. *Science* **1998**, *281*, 956−961.

(17) Akiyama, M.; Kamohara, T.; Kano, K.; Teshigahara, A.; Takeuchi, Y.; Kawahara, N. Enhancement of Piezoelectric Response in Scandium Aluminum Nitride Alloy Thin Films Prepared by Dual Reactive Cosputtering. *Adv. Mater.* **2009**, *21*, 593−596.

(18) Wang, W.; Mayrhofer, P. M.; He, X.; Gillinger, M.; Ye, Z.; Wang, X.; Bittner, A.; Schmid, U.; Luo, J. K. High performance AlScN thin film based surface acoustic wave devices with large electromechanical coupling coefficient. *Appl. Phys. Lett.* **2014**, *105*, 133502.

(19) Talley, K. R.; Sherbondy, R.; Zakutayev, A.; Brennecka, G. L. Review of high-throughput approaches to search for piezoelectric nitrides. *J. Vac. Sci. Technol. A* **2019**, *37*, 060803.

(20) Drury, D.; Yazawa, K.; Mis, A.; Talley, K.; Zakutayev, A.; Brennecka, G. L. Understanding Reproducibility of Sputter-Deposited Metastable Ferroelectric Wurtzite $Al_{0.6}Sc_{0.4}N$ Films Using In Situ Optical Emission Spectrometry. *Phys. Status Solidi RRL* **2021**, *15*, 210004.

(21) Yazawa, K.; Drury, D.; Zakutayev, A.; Brennecka, G. L. Reduced coercive field in epitaxial thin film of ferroelectric wurtzite $Al_{0.7}Sc_{0.3}N$. *Appl. Phys. Lett.* **2021**, *118*, 162903.

(22) Yazawa, K.; Zakutayev, A.; Brennecka, G. L. A Landau−Devonshire analysis of strain effects on ferroelectric $Al_{1-x}Sc_xN$. *Appl. Phys. Lett.* **2022**, *121*, 042902.

(23) Fichtner, S.; Wolff, N.; Lofink, F.; Kienle, L.; Wagner, B. AlScN: A III-V semiconductor based ferroelectric. *J. Appl. Phys.* **2019**, *125*, 114103.

(24) Yazawa, K.; Mangum, J. S.; Gorai, P.; Brennecka, G. L.; Zakutayev, A.Local chemical origin of ferroelectric behavior in wurtzite nitrides*J. Mater. Chem. C***2022**, DOI: 10.1039/D2TC02682A.

(25) Satoh, S.; Ohtaka, K.; Shimatsu, T.; Tanaka, S. Crystal structure deformation and phase transition of AlScN thin films in whole Sc concentration range. *J. Appl. Phys.* **2022**, *132*, 025103.

(26) Liu, H.; Zeng, F.; Tang, G.; Pan, F. Enhancement of piezoelectric response of diluted Ta doped AlN. *Appl. Surf. Sci.* **2013**, *270*, 225−230.

(27) Yokoyama, T.; Iwazaki, Y.; Onda, Y.; Nishihara, T.; Sasajima, Y.; Ueda, M. Effect of Mg and Zr co-doping on piezoelectric AlN thin

films for bulk acoustic wave resonators. *IEEE Trans. Ultrason. Ferroelectr. Freq. Control* **2014**, *61*, 1322−1328.

(28) Manna, S.; Brennecka, G. L.; Stevanović, V.; Ciobanu, C. V. Tuning the piezoelectric and mechanical properties of the AlN system via alloying with YN and BN. *J. Appl. Phys.* **2017**, *122*, 105101.

(29) Manna, S.; Talley, K. R.; Gorai, P.; Mangum, J.; Zakutayev, A.; Brennecka, G. L.; Stevanović, V.; Ciobanu, C. V. Enhanced Piezoelectric Response of AlN via CrN Alloying. *Phys. Rev. Appl.* **2018**, *9*, 034026.

(30) Liu, Z.; Luo, B.; Hou, B. Coexistence of ferroelectricity and ferromagnetism in Ni-doped $Al_{0.7}Sc_{0.3}N$ thin films. *Appl. Phys. Lett.* **2022**, *120*, 252904.

(31) Kabulski, A.; Pagán, V. R.; Korakakis, D. Erbium Alloyed Aluminum Nitride Films for Piezoelectric Applications. *MRS Proc.* **2009**, *1129*, 1129-V09-02.

(32) Jia, J.; Yanagitani, T. Origin of Enhanced Electromechanical Coupling in (Yb,Al)N Nitride Alloys. *Phys. Rev. Appl.* **2021**, *16*, 044009.

(33) Yanagitani, T.; Suzuki, M. Enhanced piezoelectricity in YbGaN films near phase boundary. *Appl. Phys. Lett.* **2014**, *104*, No. 082911.

(34) Teraguchi, N.; Suzuki, A.; Nanishi, Y. Growth and Characterization of GaGdN and AlGdN on SiC by RF-MBE. *Mater. Sci. Forum* **2002**, *389−393*, 1477−1480.

(35) Gruber, J. B.; Vetter, U.; Hofsäss, H.; Zandi, B.; Reid, M. F. Spectra and energy levels of Gd^{3+} ($4f^7$) in AlN. *Phys. Rev. B* **2004**, *69*, No. 195202.

(36) Kita, T.; Kitayama, S.; Kawamura, M.; Wada, O.; Chigi, Y.; Kasai, Y.; Nishimoto, T.; Tanaka, H.; Kobayashi, M. Narrow-band deep-ultraviolet light emitting device using $Al_{1−x}Gd_xN$. *Appl. Phys. Lett.* **2008**, *93*, 211901.

(37) Chen, Y.; Shi, X.; Yang, J.; Chen, Y. Growth and optical properties of gadolinium aluminum nitride thin films. *Physica Status Solidi C* **2012**, *9*, 1040−1042.

(38) Choi, S. W.; Zhou, Y. K.; Emura, S.; Lee, X. J.; Teraguch, N.; Suzuki, A.; Asahi, H. Magnetic, optical and electrical properties of GaN and AlN doped with rare-earth element Gd. *Phys. Status Solidi C* **2006**, *3*, 2250−2253.

(39) Fukui, K.; Sawai, S.; Ito, T.; Emura, S.; Araki, T.; Suzuki, A. Photoluminescence and photoluminescence excitation spectra from AlN doped with Gd^{3+}. *Phys. Status Solidi C* **2010**, *7*, 1878−1880.

(40) Han, S. Y.; Hite, J.; Thaler, G. T.; Frazier, R. M.; Abernathy, C. R.; Pearton, S. J.; Choi, H. K.; Lee, W. O.; Park, Y. D.; Zavada, J. M.; Gwilliam, R. Effect of Gd implantation on the structural and magnetic properties of GaN and AlN. *Appl. Phys. Lett.* **2006**, *88*, 042102.

(41) Kresse, G.; Furthmüller, J. Efficient iterative schemes for ab initio total-energy calculations using a plane-wave basis set. *Phys. Rev. B.* **1996**, *54*, 11169.

(42) Perdew, J. P.; Burke, K.; Ernzerhof, M. Generalized Gradient Approximation Made Simple. *Phys. Rev. Lett.* **1996**, *77*, 3865−3868.

(43) Blöchl, P. E. Projector augmented-wave method. *Phys. Rev. B* **1994**, *50*, 17953.

(44) Leuenberger, F.; Parge, A.; Felsch, W.; Fauth, K.; Hessler, M. GdN thin films: Bulk and local electronic and magnetic properties. *Phys. Rev. B* **2005**, *72*, 014427.

(45) Wachter, P. Physical and Chemical Properties of GdN: A Critical Comparison between Single Crystals and Thin Films, Theory and Experiment. *Adv. Mater. Phys. Chem.* **2016**, *6*, 28−46.

(46) Zunger, A.; Wei, S.-H.; Ferreira, L.; Bernard, J. E. Special quasirandom structures. *Phys. Rev. Lett.* **1990**, *65*, 353−356.

(47) van de Walle, A. Multicomponent multisublattice alloys, nonconfigurational entropy and other additions to the Alloy Theoretic Automated Toolkit. *Calphad* **2009**, *33*, 266−278.

(48) Talley, K. R.; Bauers, S. R.; Melamed, C. L.; Papac, M. C.; Heinselman, K. N.; Khan, I.; Roberts, D. M.; Jacobson, V.; Mis, A.; Brennecka, G. L.; Perkins, J. D.; Zakutayev, A. COMBIgor: Data-analysis package for combinatorial materials science. *ACS Comb. Sci.* **2019**, *21*, 537−547.

(49) Zakutayev, A.; Wunder, N.; Schwarting, M.; Perkins, J. D.; White, R.; Munch, K.; Tumas, W.; Phillips, C. An open experimental database for exploring inorganic materials. *Sci. Data* **2018**, *5*, 180053.

(50) Talley, K. R.; White, R.; Wunder, N.; Eash, M.; Schwarting, M.; Evenson, D.; Perkins, J. D.; Tumas, W.; Munch, K.; Phillips, C.; Zakutayev, A. Research data infrastructure for high-throughput experimental materials science. *Patterns* **2021**, *2*, 100373.

(51) Toby, B. H.; Von Dreele, R. B. *GSAS-II*: the genesis of a modern open-source all purpose crystallography software package. *J. Appl. Crystallogr.* **2013**, *46*, 544−549.

(52) Kieffer, J.; Valls, V.; Blanc, N.; Hennig, C. New tools for calibrating diffraction setups. *J. Synchrotron Radiat.* **2020**, *27*, 558−566.

(53) Lilliu, S.; Dane, T.Reciprocal Space Mapping for Dummies, arXiv (Soft Condensed Matter) 1511.06224, arXiv.org e-Print archive, 2015. https://doi.org/10.48550/arXiv. (accessed July 11, 2022).

(54) Motamedi, P.; Cadien, K. Structural and optical characterization of low-temperature ALD crystalline AlN. *J. Cryst. Growth* **2015**, *421*, 45−52.

(55) Liu, Y.; Li, Q. X.; Wan, L. Y.; Kucukgok, B.; Ghafari, E.; Ferguson, I. T.; Zhang, X.; Wang, S.; Feng, Z. C.; Lu, N. Composition and temperature dependent optical properties of $Al_xGa_{1−x}N$ alloy by spectroscopic ellipsometry. *Appl. Surf. Sci.* **2017**, *421*, 389−396.

(56) Cordell, J. J.; Pan, J.; Tamboli, A. C.; Tucker, G. J.; Lany, S. Probing configurational disorder in $ZnGeN_2$ using cluster-based Monte Carlo. *Phys. Rev. Mater.* **2021**, *5*, 024604.

(57) Han, M.; Yan, J.; Granick, S.; Luijten, E. Effective temperature concept evaluated in an active colloid mixture. *Proc. Natl. Acad. Sci. U.S.A.* **2017**, *114*, 7513−7518.

(58) Song, C.; Wang, P.; Makse, H. A. Experimental measurement of an effective temperature for jammed granular materials. *Proc. Natl. Acad. Sci. U.S.A.* **2005**, *102*, 2299−2304.

(59) Cross, M. C.; Hohenberg, P. C. Pattern formation outside of equilibrium. *Rev. Mod. Phys.* **1993**, *65*, 851−1112.

(60) Greenaway, A. L.; Loutris, A. L.; Heinselman, K. N.; Melamed, C. L.; Schnepf, R. R.; Tellekamp, M. B.; Woods-Robinson, R.; Sherbondy, R.; Bardgett, D.; Bauers, S.; Zakutayev, A.; Christensen, S. T.; Lany, S.; Tamboli, A. C. Combinatorial Synthesis of Magnesium Tin Nitride Semiconductors. *J. Am. Chem. Soc.* **2020**, *142*, 8421−8430.

(61) Talley, K. R.; Perkins, C. L.; Diercks, D. R.; Brennecka, G. L.; Zakutayev, A. Synthesis of $LaWN_3$ nitride perovskite with polar symmetry. *Science* **2021**, *374*, 1488−1491.

(62) Kitayama, S.; Kita, T.; Kawamura, M.; Wada, O.; Chigi, Y.; Kasai, Y.; Nishimoto, T.; Tanaka, H.; Kobayashi, M. Narrowband ultraviolet field-emission device using Gd-doped AlN. *IOP Conf. Ser.: Mater. Sci. Eng.* **2009**, *1*, 012001.

(63) CrystalMaker: a powder diffraction program for Mac and Windows. CrystalMaker Software Ltd, Oxford, England, www.crystalmaker.com.

(64) Iwahashi, S.; Kishi, N.; Kitayama, S.; Kita, T.; Chigi, Y.; Nishimoto, T.; Tanaka, H.; Kobayashi, M.; Ishihara, T.; Izumi, H. Multiple excitation process in deep-ultraviolet emission from AlGdN thin films pumped by an electron beam. *J. Appl. Phys.* **2012**, *111*, 083526.

(65) Choi, S. W.; Emura, S.; Kimura, S.; Kim, M. S.; Zhou, Y. K.; Teraguchi, N.; Suzuki, A.; Yanase, A.; Asahi, H. Emission spectra from AlN and GaN doped with rare earth elements. *J. Alloys Compd.* **2006**, *408−412*, 717−720.

(66) Vetter, U.; Zenneck, J.; Hofsäss, H. Intense ultraviolet cathodoluminescence at 318 nm from Gd^{3+}-doped AlN. *Appl. Phys. Lett.* **2003**, *83*, 2145−2147.

(67) Shannon, R. D. Revised effective ionic radii and systematic studies of interatomic distances in halides and chalcogenides. *Acta Crystallogr., Sect. A* **1976**, *32*, 751−767.

(68) Talley, K. R.Investigation of Potential Piezoelectric Nitride Materials via Combinatorial Methods, PhD Thesis Proposal; Colorado School of Mines: Golden, CO, 2018.

(69) Jia, J.; Iwata, N.; Suzuki, M.; Yanagitani, T. Enhanced Electromechanical Coupling in Yb-Substituted III-V Nitride Alloys. *ACS Appl. Electron. Mater.* **2022**, *4*, 3448−3456.

📖 Recommended by ACS

Effect of Intrinsic and Extrinsic Oxygen Vacancies on the Conductivity of Gd-Doped CeO₂ Synthesized by a Sonochemical Route

Taranveer Kaur, Jayant Kolte, *et al.*
OCTOBER 17, 2022
THE JOURNAL OF PHYSICAL CHEMISTRY C

READ 🗗

Metastable γ-Li₂TiTeO₆: Negative Chemical Pressure Interception and Polymorph Tuning of SHG

Mei-Huan Zhao, Man-Rong Li, *et al.*
NOVEMBER 07, 2022
CHEMISTRY OF MATERIALS

READ 🗗

Effects of Ga Substitution on the Local Structure of Na₂Zn₂TeO₆

Frida Sveen Hempel, Helmer Fjellvåg, *et al.*
AUGUST 09, 2022
INORGANIC CHEMISTRY

READ 🗗

Triple A-Site Cation Ordering in the Ferrimagnetic Y₂CuGaMn₄O₁₂ Perovskite

Alexei A. Belik, Kazunari Yamaura, *et al.*
AUGUST 31, 2022
INORGANIC CHEMISTRY

READ 🗗

Get More Suggestions >